Supplementary Information (SI) for Digital Discovery.

Supplementary Information

ALBATROSS: A robotised system for high-throughput electrolyte screening via automated electrolyte formulation, coin-cell fabrication, and electrochemical evaluation

Hyun-Gi Lee[1‡], Jaekyeong Han[1‡], Minjun Kwon[1], Hyeonuk Kwon[2],

Jooha Park[3], Hoe Jin Ha[3], Dong-Hwa Seo[1, 2*]

[1]Department of Materials Science and Engineering, Korea Advanced Institute of Science and Technology (KAIST), Daejeon, 34141, Republic of Korea

[2]Graduate School of Green Growth and Sustainability, Korea Advanced Institute of Science and Technology (KAIST), Daejeon, 34141, Republic of Korea

[3]LG Energy Solution, Seoul, 07796, Republic of Korea

‡These authors contributed equally: Hyun-Gi Lee and Jaekyeong Han

Corresponding Authors: *e-mail: dseo@kaist.ac.kr (Prof. D.-H. Seo)

1. Electrolyte Preparation

Electrolyte formulation was performed using the liquid handler robot. Although lithium salts are typically supplied in powder form and must be weighed and dissolved in solvents to prepare solutions, automating the precise dispensing of powder within the confined space of the glovebox is challenging. To overcome this limitation, electrolyte solutions were prepared by diluting prepared concentrated salt solutions with pure solvents. Since higher solubility allows for a wider range of electrolyte combinations, solvent selection should be carefully considered. For solvents such as ethylene carbonate (EC), which is solid at room temperature, a temperature-control module was employed to maintain the solvent at 60°C prior to dispensing. To eliminate the risk of cross-contamination, a new pipette tip is used for every solution transfer and mixing step. During solution dispensing with an automated micropipette integrated within the liquid handler, excess solution adhering to the pipette tip was removed by touching the tip to the vial entrance. The solutions were then mixed using the automated micropipette, performing 20 repetitive mixing strokes over a total duration of 3 minutes.

To evaluate the validity of the dilution method for electrolyte preparation, two tests were conducted: (1) assessing whether accurate volumetric dispensing is achievable using water as a model system, and (2) preparing solutions of 1 M $LiPF_6$ in EC and 3 M $LiPF_6$ in dimethyl carbonate (DMC), which were subsequently diluted with pure EC and DMC to obtain various electrolyte compositions.

For the first test, experiments were performed under the same conditions specified by the Opentrons system validation protocol, using a 300 µL pipette to dispense 20, 150, and 300 µL of water at room temperature. The results confirmed sufficient accuracy and reproducibility (Table S1). For the second test, each solution was prepared in duplicate, and the $LiPF_6$ concentration as well as the EC/DMC volume ratio were analyzed by ^1H NMR and ^{19}F NMR spectroscopy. Minor deviations were observed when the electrolyte contained a high proportion of EC, attributable to its high viscosity. However, when low-viscosity solvents dominated the mixture, the error was significantly reduced. Given the small variability between replicates, the dilution approach is suitable for automated electrolyte preparation (Table S2).

Volume [ul]	1	2	3	4	5	6	7	8	9	10	Mean	Accuracy	Precision
0.02	0.0199	0.0206	0.0198	0.0205	0.0208	0.0190	0.0197	0.0203	0.0195	0.0206	**0.0201**	**0.55%**	**2.91%**
0.15	0.1462	0.1467	0.1467	0.1473	0.1476	0.1480	0.1494	0.1463	0.1470	0.1463	**0.1471**	**-1.90%**	**0.67%**
0.3	0.3021	0.3030	0.3035	0.3053	0.3033	0.3000	0.3059	0.2997	0.3000	0.2993	**0.3022**	**0.74%**	**0.79%**

Table S1. Results of the liquid handler volume dispensing performance. Water was dispensed at room temperature condition.

Target value			Result			Error		Standard Dev.	
$LiPF_6$ conc.	EC vol%	DMC vol%	$LiPF_6$ conc.	EC vol%	DMC vol%	conc. error	vol% error	conc. std.	vol% std.
1 M	70%	30%	1.07 M	71.36%	28.64%	7.0%	±1.36%	0.0283 M	0.8839%
			1.11 M	70.11%	29.89%	11.0%	±0.11%		
1 M	50%	50%	1.04 M	47.54%	52.46%	4.0%	±2.46%	0.0071 M	0.4031%
			1.05 M	48.11%	51.89%	5.0%	±1.89%		
1 M	30%	70%	1.04 M	28.99%	71.01%	4.0%	±1.01%	0.0212 M	0.0495%
			1.01 M	28.92%	71.08%	1.0%	±1.08%		

Table S2. Results of electrolyte formulation test. The solutions were formulated by mixing 1M $LiPF_6$ in EC, 3M $LiPF_6$ in DMC, pure EC and pure DMC. H-NMR and F-NMR analyses are conducted to analyze concentration of $LiPF_6$ and vol% of EC and DMC.

2. Cell component and Assembly assisting structures

The automated coin-cell assembly process is divided into three main stages: component transfer, electrolyte dispensing, and cell crimping. The cell components include the can, anode, separator, electrolyte, cathode, spacer, spring, gasket, and cap. Within the limited space of the glovebox, it is challenging for the robot arm to manipulate components if they are dispersed across multiple positions. To address this issue, all components were fixed at designated positions to ensure reliable robot access. The components were categorized into two groups: stackable components (can, cap, spacer) and non-stackable components (cathode, anode, separator, wave spring) (Fig. S1). Stackable components were arranged in stacks of 12 units. After one component was retrieved by the robot arm, the next was elevated using an actuator to maintain a constant supply position. For non-stackable components, a rotary indexing table driven by a stepper motor was employed. 12 units of each type were positioned on a circular plate, and as each component was used, the plate was rotated to present the next component to the robot arm (Fig. S2). This configuration fixed all components at accessible positions, simplified robotic calibration to a single coordinate per component and facilitated system maintenance. Once a plate of 12 components was fully consumed, it was replaced with a new plate by the robot arm. To streamline this replacement, a dedicated storage structure, called a plate stacker, was fabricated to hold multiple pre-loaded plates in a stacked configuration, ensuring that each plate could be consistently positioned for retrieval by the robot arm (Fig. S3).

The assembly process was carried out on an assembly post located inside the liquid handler, which enabled dispensing of 70 µL of electrolyte directly into each partially assembled cell. A camera was installed above the assembly post to record each transfer step and to verify the correct placement of components. An actuator positioned below the assembly post was used to adjust component alignment and to elevate stacked cells, allowing the robot gripper to securely grab and transfer them to the cell crimper. At the crimping stage, cells were mechanically sealed using the automated crimper. After crimping, the assembled coin cell was retrieved by a vacuum gripper and transferred to the cycling gantry system for electrochemical testing.

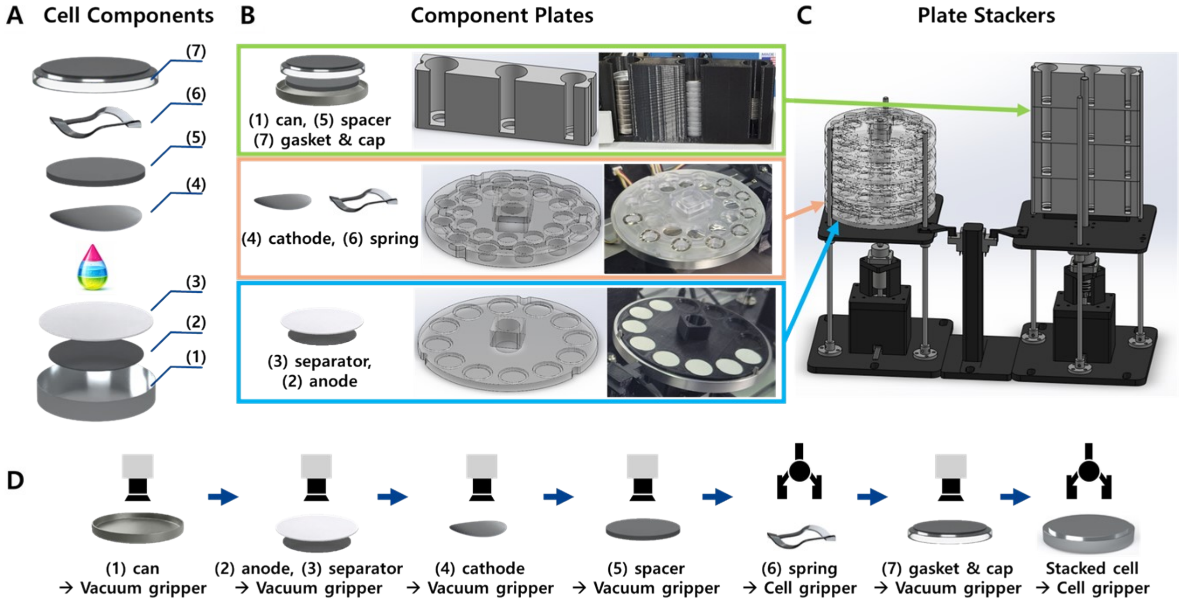

Figure S1. (A) Illustration of coin cell components: (1) can (2) anode (3) separator (4) cathode (5) spacer (6) wave spring (7) gasket & cap. (B) Schematic of customized component plates: a stacking plate for the can, cap, and spacer; a circular plate for the cathode and wave spring; and a separate circular plate for the anode and separator. (C) Figure of plate stackers for component plates. (D) Illustration of how cell components are handled.

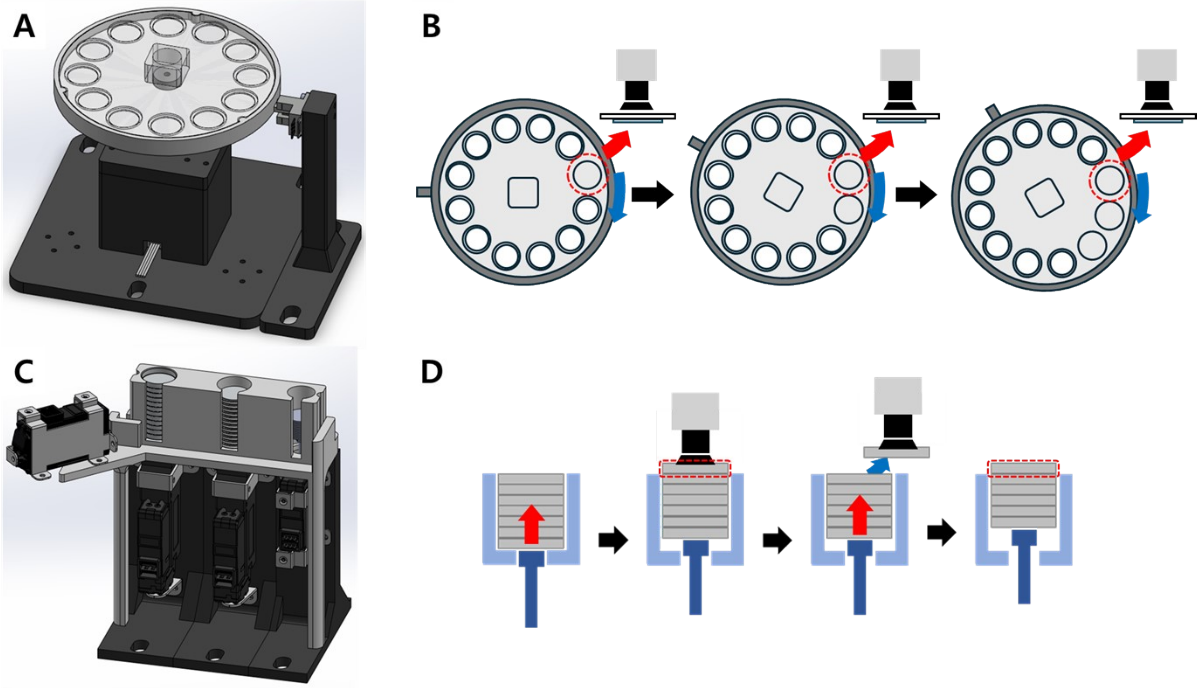

Figure S2. (A) Figure of a rotary indexing table for a circular component plate. (B) Illustration of supply a new component using a rotary indexing table. (C) Figure of actuator structure for a stacking component plate. (D) Illustration of supply a new component by pushing up the components using actuators.

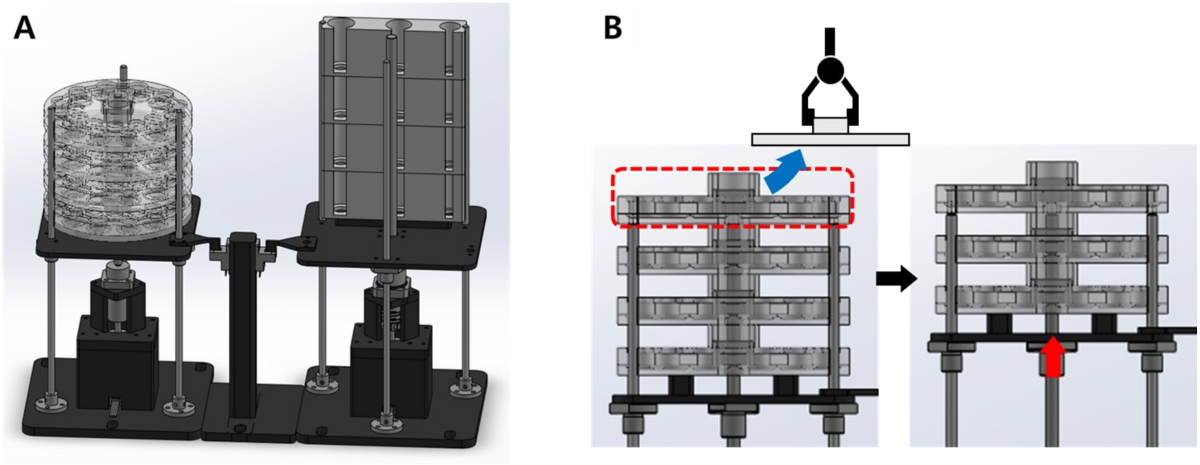

Figure S3. (A) Figure of plate stackers using linear motors. (B) Illustration of supply of a new component plate by pushing up the plates.

3. Robot Gripper

The transfer of cell components was carried out using the robot arm equipped with a custom-designed gripper. To fabricate the gripper with the simplest form capable of handling diverse components, multiple prototypes were 3D printed and tested, after which a final customized design was selected and utilized. The gripper consisted of three modules: a cell transfer unit, a vacuum gripper unit, and a parallel gripper unit (Fig. S4). Most components including the can, anode, separator, cathode, spacer, gasket, and cap were transported using the vacuum gripper unit. The wave spring and stacked cells were handled using the cell transfer unit, while the component plates were handled using the parallel gripper unit. The vacuum gripper unit was connected to a digital pressure sensor to detect whether an object was successfully grasped. If the object was not firmly grabbed, the robot arm went down 0.1 mm until grabbing was achieved. Once the object was grasped, the downward motion stopped and transfer was initiated. If the object was not obtained after a 1.5 mm descent, the system entered an error state and halted operation (Fig. S5). This vacuum grasping protocol significantly improved the reliability of the vacuum gripper and ensured stable and accurate transfer of components.

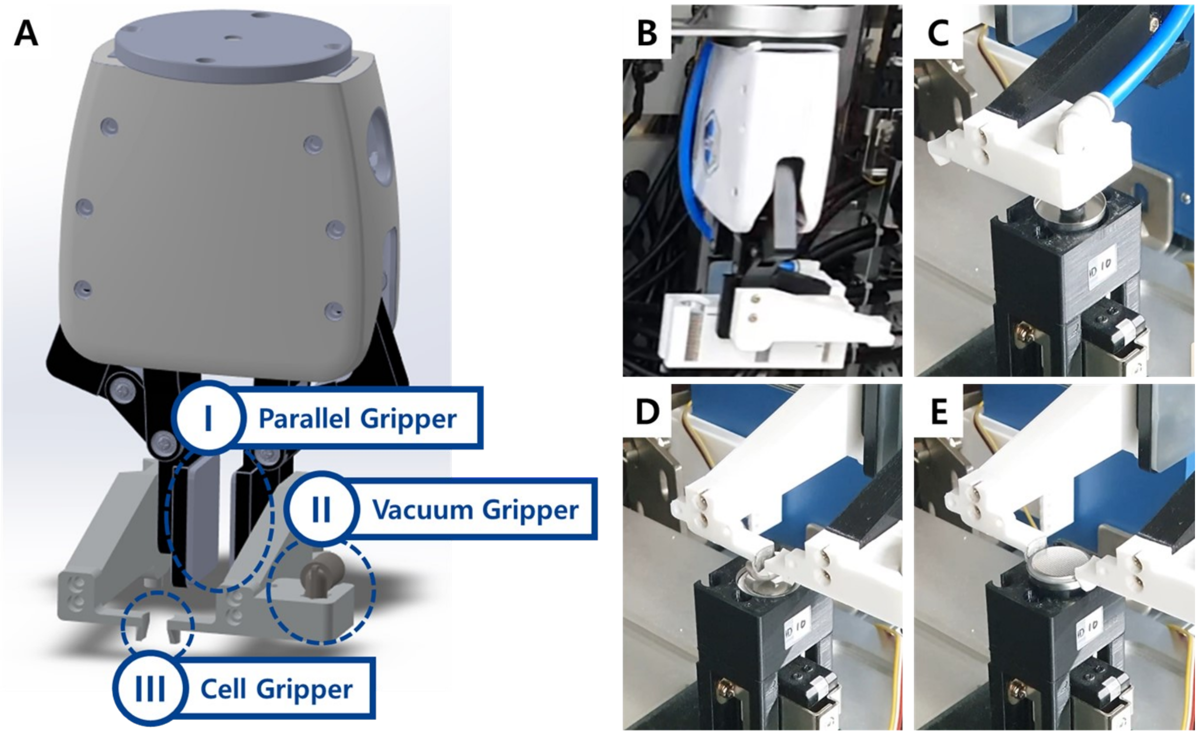

Figure S4. (A) Schematic illustration of the designed gripper for robot arm. (B) Figure of handling the plate using the parallel gripper (I). (C) Figure of moving a can using the vacuum gripper (II). (D) Figure of moving a wave spring and (E) a stacked cell using the cell gripper (III).

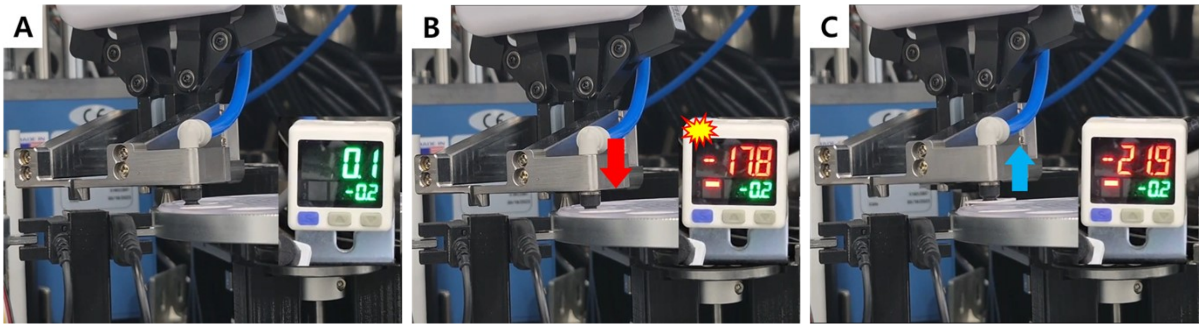

Figure S5. Illustration of how the vacuum gripper grabs the component. (A) The robot arm moves to a designated position. (B) Then the robot arm moves down until a digital pressure gauge detects the grabbing. (C) The robot arm moves the component to adequate position.

4. Electrochemical Characterization

The automation of electrochemical characterization began with the placement of assembled cells onto the cycling gantry. After cell placement, the gantry identified vacant positions among the 48 jigs and inserted the cells accordingly. In addition to the 48 cycling jigs, two EIS jigs were installed, allowing cells to be retrieved from their cycling jigs and inserted into the EIS analyzing jigs for impedance measurements and subsequently returned to their original positions (Figs. S6, S7). This configuration enabled the acquisition of data related to degradation during cycling, while operating independently of the robot arm, thereby enhancing overall efficiency. After the completion of cycling and impedance measurements, the cycling gantry retrieved the cells and positioned them in locations accessible to the robot arm. The robot arm then either discarded the cells or transferred them to a storage plate for further analysis.

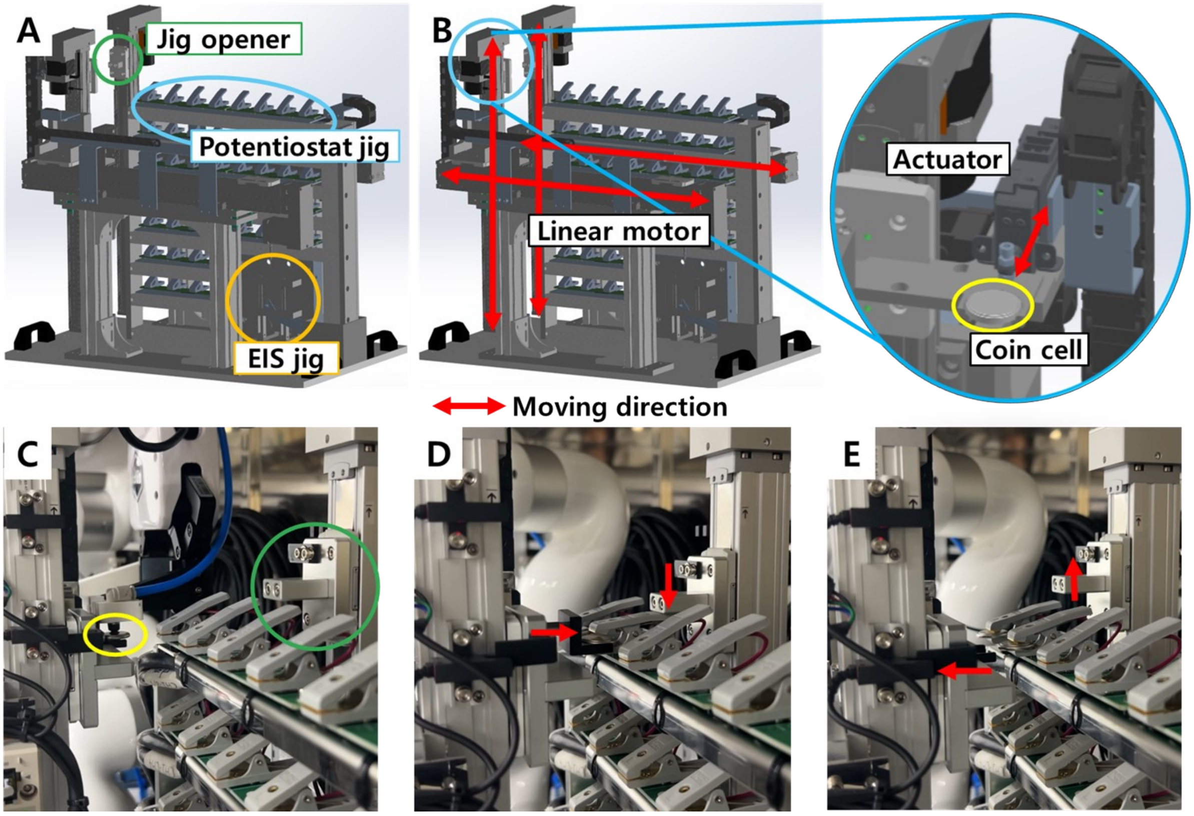

Figure S6. (A) Illustration of coin-cell cycling system. The system is composed of two gantry systems, 48 potentiostat jigs and 2 EIS jigs. (B) One gantry moves the coin cell to the jig, and the other gantry opens the jig. (C) Figure of showing the robot arm moves the cell into the gantry system, (D) cell transportation to the potentiostat jig, and (E) retrieve actuator after cell transportation.

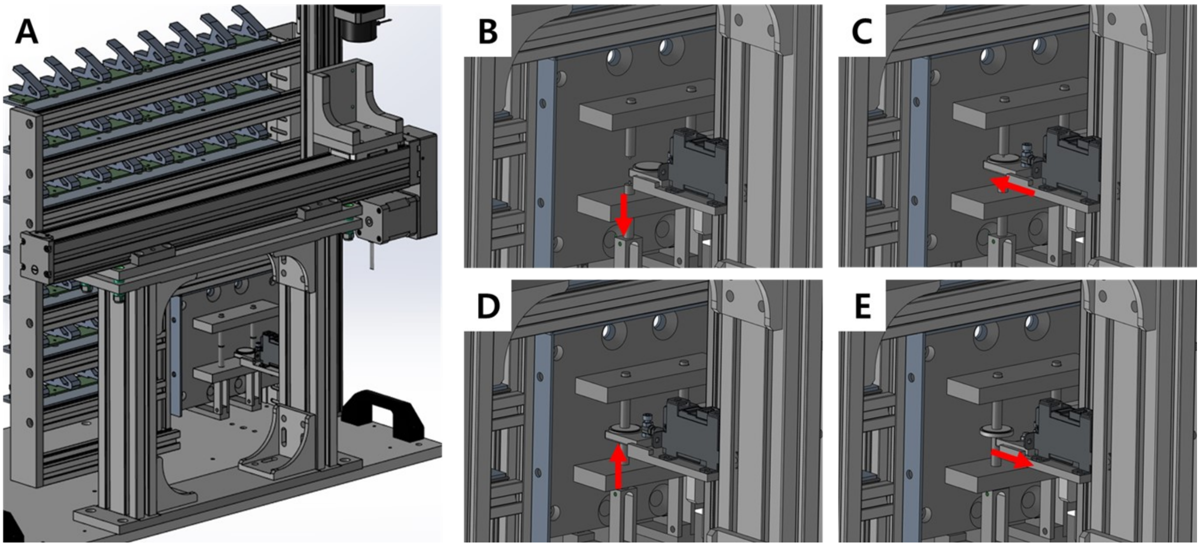

Figure S7. (A) Illustration of EIS automation process. (B) An actuator opens the EIS jig. (C) Another actuator inserts the cell into the jig. (D) The actuator closes the jig. (E) The actuator retracts and goes back to origin position.

5. Scheduling the automation

To enhance the throughput of cell assembly, the three main processes (electrolyte preparation, cell assembly, and electrochemical testing) had to be operated in parallel. This required a central controller capable of monitoring and coordinating the progress of each process. A Programmable Logic Controller (PLC) was employed for this purpose, as it is appropriate for real-time control and synchronization of multiple devices. Operating independently of the main PC, the PLC supported various communication protocols, enabling direct communication and control of stepper motors, photo sensors, actuators, the robot arm, and the main PC itself. Since the liquid handler and cyclers did not provide communication protocols, they were directly controlled through Python programs running on the main PC (Fig. S8). Communication between the PLC and PC was established using OPC UA, with the PC submitting jobs to the PLC, which then queried device status and orchestrated the overall workflow. The PLC exposed device-related operational variables through an OPC UA server, enabling efficient communication. As a result, these variables could be readily read and written via Python, allowing convenient monitoring of real-time system status and the transmission of control commands.

To prevent equipment collisions, the PLC implemented interlocks that temporarily halted operations until potential conflicts were resolved. For example, when the liquid handler was injecting electrolyte into a coin cell, the robot arm was prevented from transferring additional components onto the assembly post. Similarly, when the robot arm was transporting a cell to the cycling gantry, the gantry was restricted from initiating motion. These safeguards ensured reliable and safe automation of the integrated system. To enable such coordinated operation, an interlock architecture was implemented within the PLC. These interlock signals were also exposed as external variables and could be accessed and modified via OPC UA communication. Interlocks were assigned to each major module, including the liquid handler, crimper, cycling test module, and robot arm, and the corresponding variables could be monitored and updated at any time by either the Python control program or the PLC. This architecture prevented operational conflicts when multiple modules were active simultaneously, thereby enabling efficient parallel task execution.

To control ALBATROSS, two Python programs were employed: (1) a cell assembly code and (2) an EIS automation code. The user primarily interacts with the cell assembly code by providing operational parameters, such as the number of cells to be assembled, the electrolyte reservoir position, the dispensing protocol, and the number of spare pipette tips. These execution parameters are transmitted via the Python interface.

The cell assembly code communicates with both the PLC and the liquid handler. Upon receiving the input parameters, the PLC organizes and coordinates commands for the cell assembly module, including the robot arm. Tasks related to electrolyte handling are executed through direct communication between the Python code and the liquid handler.

In contrast, the EIS automation code operates continuously in the background. This program monitors the status of cells connected to the cycler in real time and identifies those ready for EIS measurement. When a specific cell completes a 30-minute rest period and enters a pause state, the code sends a command to the PLC to transfer the cell to the EIS jig for impedance measurement. After the measurement is completed, the acquired data are stored in the main computer's data storage. The cell is then returned to its original cycling channel, the pause state is released, and cycling resumes. Once cycling is fully completed, the cycling data are also saved to the data storage (Fig. S9).

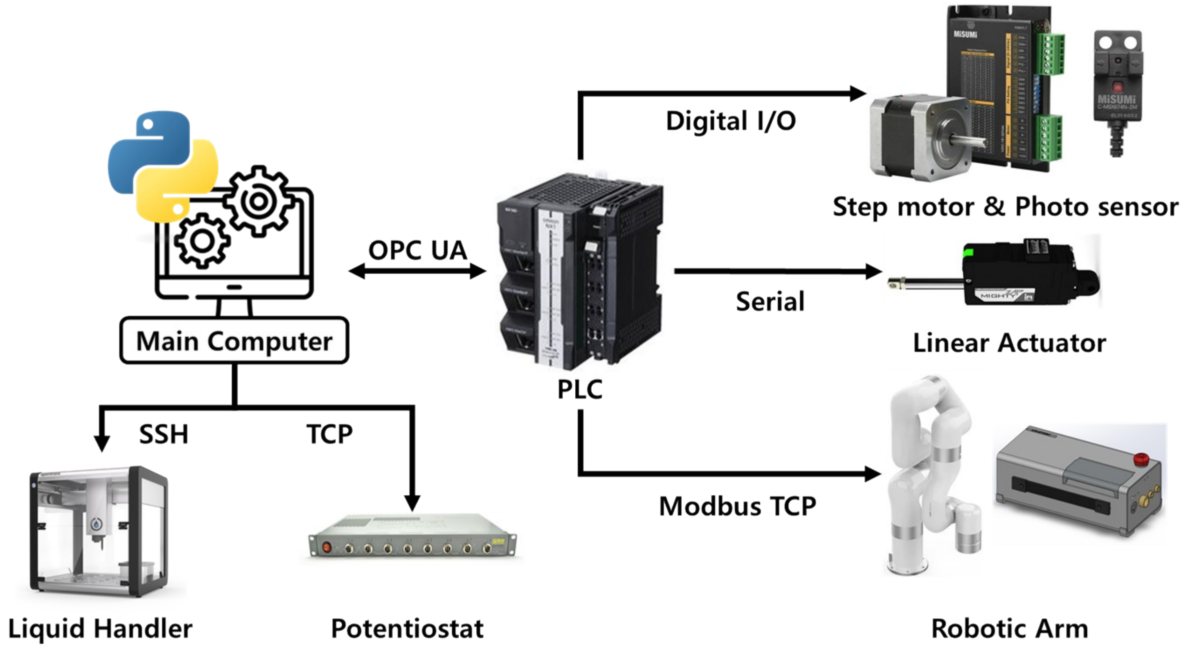

Figure S8. Illustration of operating system of automatic coin-cell test setup. To parallelly activate the modules, PLC was used, which can support various types of communication simultaneously. The liquid handler and potentiostat have their own communication method, so they communicate with the main PC directly.

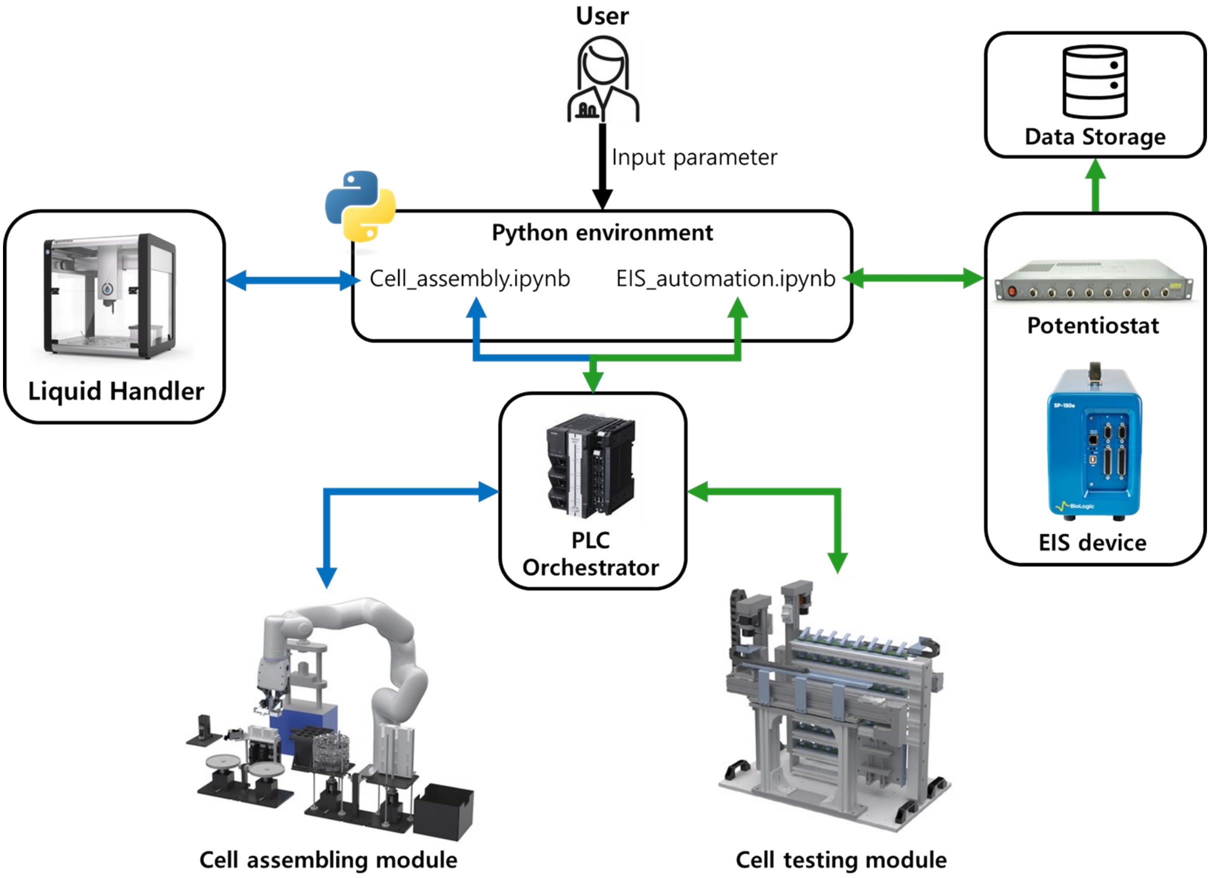

Figure S9. Schematic overview of the PLC-based operating architecture of ALBATROSS.

6. Cell assembly results

ALBATROSS requires approximately 4 minutes to assemble a single cell and can assemble up to 48 cells without researcher intervention. To evaluate assembly success rate and reproducibility across a large number of cells, 87 cells were assembled using 12.5 mm diameter NCM811 (MTI) cathodes and 120 cells using 12.5 mm diameter NCM811 (Wellcos) cathodes. The anode was a 16 mm diameter, 0.1 mm thick lithium metal foil (Honjo). A 19 mm diameter glass fiber separator (Whatman) was employed, and each cell was filled with 70 μL of electrolyte composed of 1 M $LiPF_6$ in EC:EMC (3:7 vol%) with 2 wt% VC additives (EnChem).

Among the first 87 cells assembled, two assembly failures occurred. Inspection of the two cells that failed to undergo cycling test, based on photographs taken during the assembly process, revealed that the wave spring had not been properly inserted (Fig. S10). Repeated testing of the spring transfer process indicated that the transfer failure was intermittently caused by spring detachment. This issue occurred when the cell gripper picked up the wave spring and the spring came into contact with the inner wall of the circular component plate, causing it to disengage. To address this issue, the robot arm motion was refined. Considering that the gripper expands inward to grip the spring, thereby preventing detachment during gripping, the motion path was modified such that, after grasping the spring, the gripper was moved slightly laterally to prevent collision with the plate wall. As a result, no spring detachment was observed in the subsequent 120 cells.

In terms of cell reproducibility, the MTI cathodes exhibited higher reproducibility than the Wellcos cathodes (Figs. S11, S12). This difference is attributed to electrode curling (Fig. S13). Due to differences in electrode loading level and calendering pressure, the Wellcos electrodes exhibited more pronounced curling than the MTI electrodes. Nevertheless, ALBATROSS consistently placed components at fixed positions with high positional precision, enabling precise component placement regardless of the degree of electrode curling. This demonstrates that the robotic system can mitigate electrode misalignment, commonly encountered by researchers when handling highly curled electrodes, through precise and repeatable positioning.

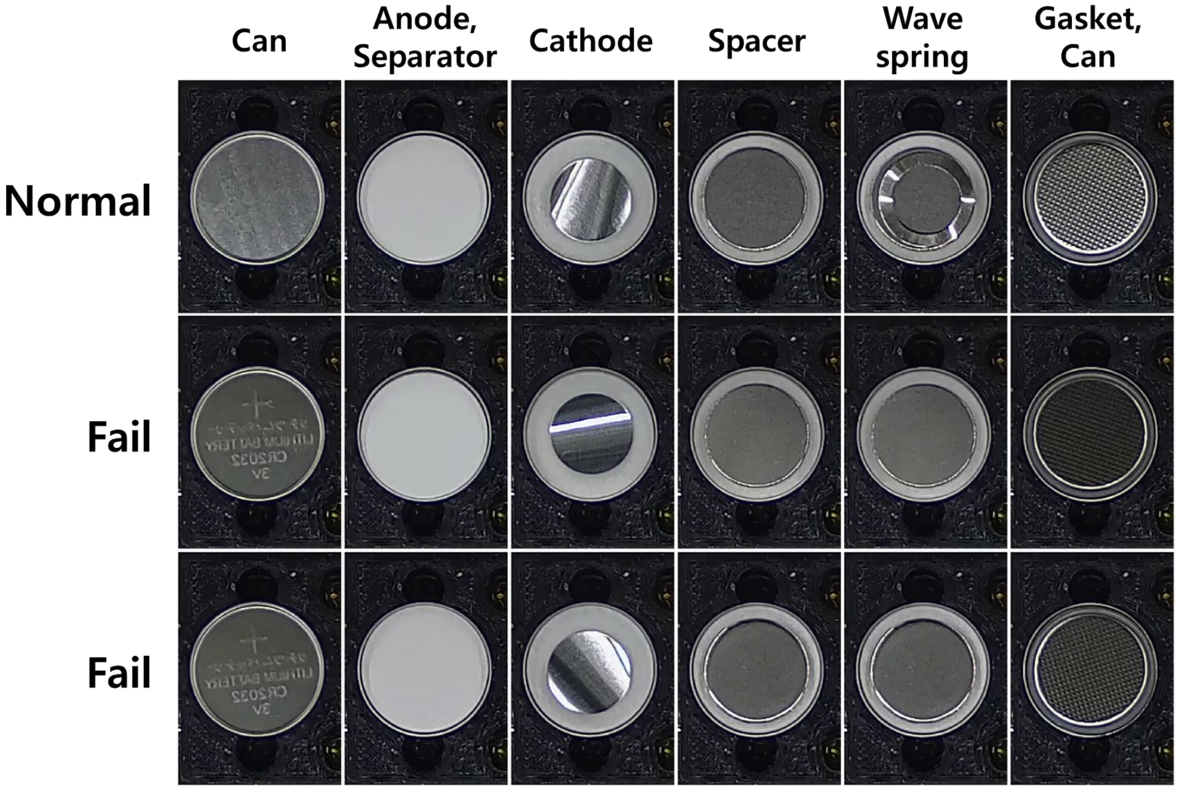

Figure S10. Photographs showing examples of component transfer failure observed during repeated assembly tests using the MTI cathodes.

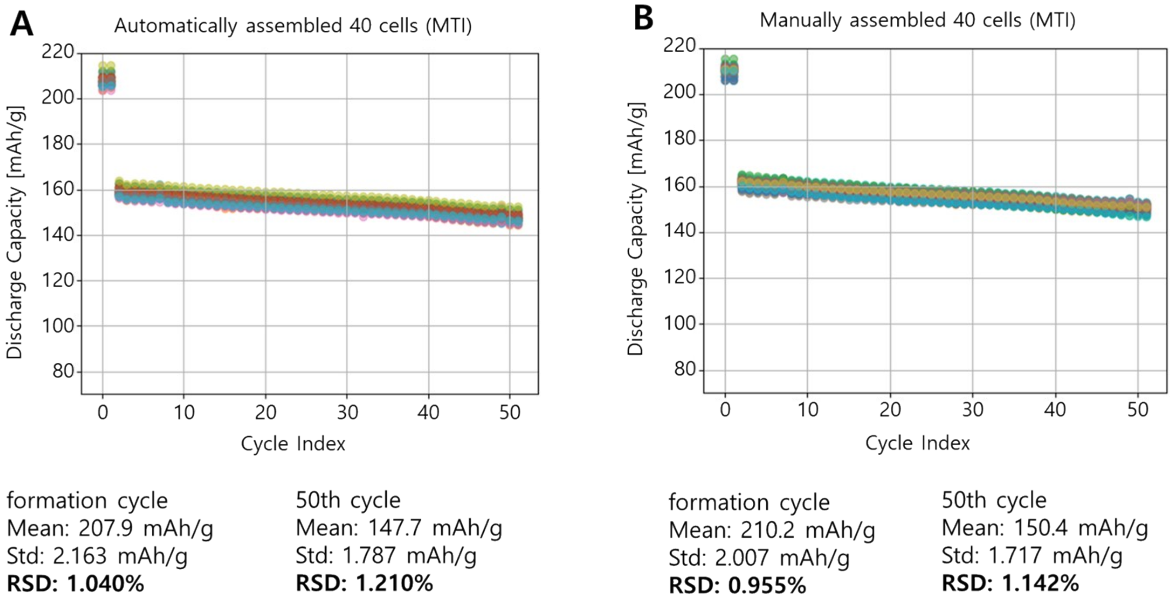

formation cycle
Mean: 207.9 mAh/g
Std: 2.163 mAh/g
RSD: 1.040%

50th cycle
Mean: 147.7 mAh/g
Std: 1.787 mAh/g
RSD: 1.210%

formation cycle
Mean: 210.2 mAh/g
Std: 2.007 mAh/g
RSD: 0.955%

50th cycle
Mean: 150.4 mAh/g
Std: 1.717 mAh/g
RSD: 1.142%

Figure S11. Discharge capacity reproducibility of 40 robot-assembled and 40 manually assembled cells using MTI cathodes.

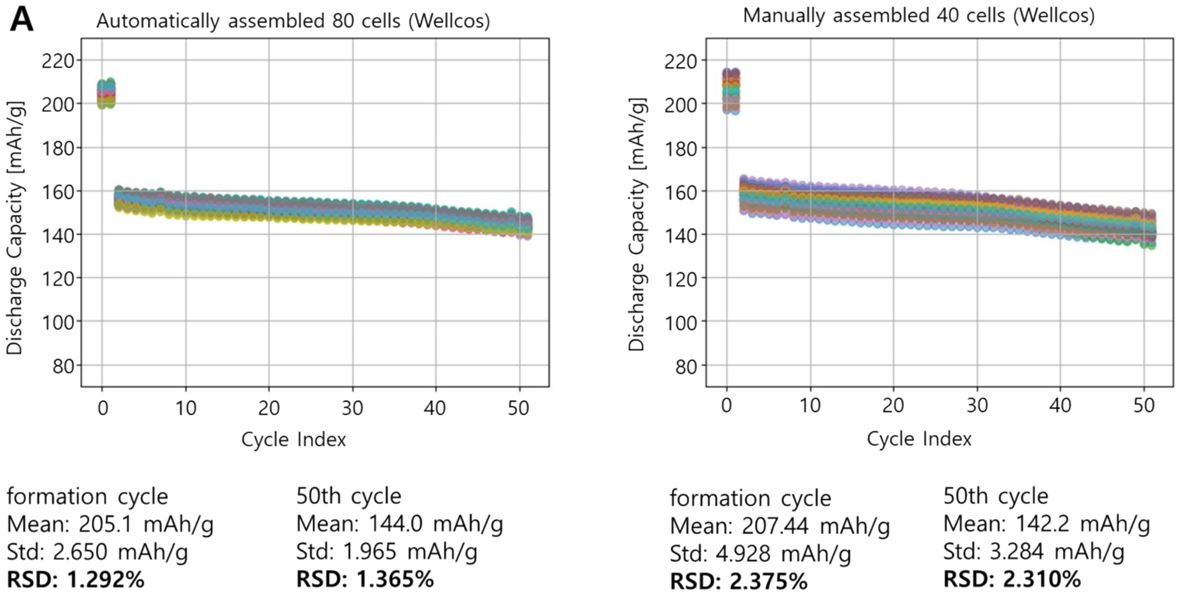

formation cycle
Mean: 205.1 mAh/g
Std: 2.650 mAh/g
RSD: 1.292%

50th cycle
Mean: 144.0 mAh/g
Std: 1.965 mAh/g
RSD: 1.365%

formation cycle
Mean: 207.44 mAh/g
Std: 4.928 mAh/g
RSD: 2.375%

50th cycle
Mean: 142.2 mAh/g
Std: 3.284 mAh/g
RSD: 2.310%

Figure S12. Discharge capacity reproducibility of 80 robot-assembled and 40 manually assembled cells using Wellcos cathodes.

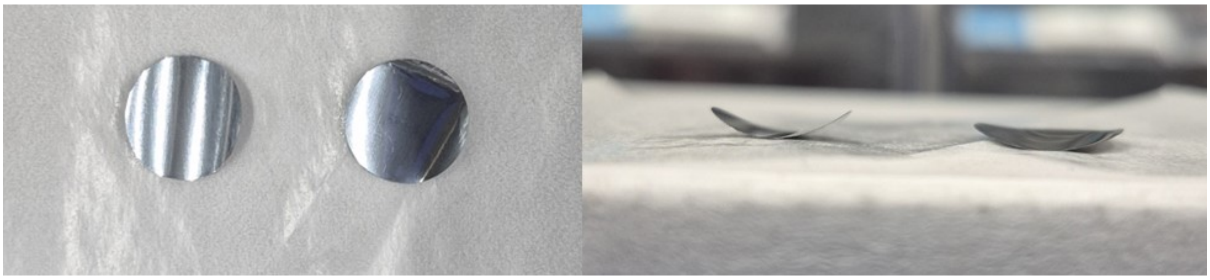

Figure S13. Photographs showing the degree of electrode curling for NCM811 cathodes from Wellcos (left) and MTI (right).

7. Impedance spectroscopy measurement

Electrochemical impedance spectroscopy (EIS) measurements were performed for 40 cells after a 12-hour rest period and the completion of two cycles at 1, 2, and 3 C-rates, following a 30-minute rest period (Figs. S14–S17). If two cells enter the EIS-measurement waiting status simultaneously, the second cell initiates its EIS measurement immediately after the first cell completes its measurement. The measurements were conducted over a frequency range of 200 kHz to 0.1 Hz, and the impedance data were analyzed using the EC-Lab software.

The EIS data were analyzed based on an equivalent circuit model composed of one ohmic resistance (R_1, R_{bulk}), two parallel RC elements representing the SEI resistance (R_2, R_{SEI}), and charge-transfer resistance (R_3, R_{CT}), and a constant phase element (CPE) element replacing Warburg impedance element. For cells measured after a 12-hours rest period, the SEI resistance was not observed; therefore, the equivalent circuit was simplified to consist of one ohmic resistance (R_1, R_{bulk}), one RC elements representing charge-transfer resistance (R_3, R_{CT}), and a constant phase element (CPE) element replacing Warburg impedance element. Mean, standard deviation, and relative standard deviation (RSD) values were calculated from analyzed data.

It is required to have suitable resting time before EIS measurement. Once the resting period begins after cycling, a cell initially in a non-equilibrium state gradually relaxes toward electrochemical equilibrium. During this relaxation process, both the open-circuit voltage (OCV) and associated resistance components evolve simultaneously. Therefore, the stabilization time prior to EIS measurement is closely correlated with the reliability and reproducibility of the impedance results. In our cycling protocols (3.0–4.2 V), the cell exhibits significant voltage recovery immediately after discharge (Fig. S18). When the discharge is terminated at 3.0 V, the cell voltage recovers to approximately 3.6 V, with the most rapid change occurring within the first 30 minutes of rest.

To quantitatively evaluate this effect, we conducted a time-dependent study on a single cell following 3C cycling. OCV and EIS measurements were repeatedly performed from 1 minute after discharge (the minimum transfer time required to move the cell from the potentiostat to the EIS jig) up to 210 minutes, at 3.5-minute intervals. The data clearly showed substantial variations in OCV and impedance values during the first 30 minutes. Therefore, a 30-minute rest period was adopted prior to EIS measurements for all cells (Fig. S19).

As the C-rate increased from 1C to 3C, both the bulk and SEI resistances tended to increase, while the charge-transfer resistance decreased. The increases in bulk and SEI resistance are likely due to the formation of dead lithium and morphological changes in the SEI layer during degradation, whereas the reduction in charge-transfer resistance is attributed to the increased reaction kinetics at higher cycling rates (Figs. S14–S17).

The current EIS measurement module has two limitations: (1) significant variation in rest time, and (2) insufficiently precise temperature control.

(1) Because up to 48 cells can complete cycling simultaneously, the number of EIS channels is smaller than that of the cycling channels, and the Cartesian robot transporting the cells operates at a deliberately slow speed for safety reasons, the actual rest time varied from 30 to 200 minutes. This limitation should be addressed in future work through improvements to the Cartesian robot system. (Fig. S20).

(2) Additionally, precise temperature control of the cycling module installed inside the large glovebox was limited. The glovebox is equipped with both heating and cooling functions to maintain a controlled environment. However, due to the relatively large internal volume of the glovebox, maintaining a perfectly uniform and constant temperature throughout the entire space remains technically challenging under the current setup. To more clearly evaluate the effect of rest-time variation, the EIS data were analyzed together with the temperature data. A noticeable correlation trend between temperature variation and changes in the EIS response was observed. This variability highlights the need for improved temperature regulation in future system upgrades (Fig. S21).

Although the aforementioned limitations remain for obtaining highly precise impedance data, the current system provides a systematic framework capable of storing and managing both temperature and impedance data. Therefore, the current platform is considered suitable for high-throughput screening applications. Further improvements will be implemented in future system configurations to enhance the clarity and stability of EIS measurements.

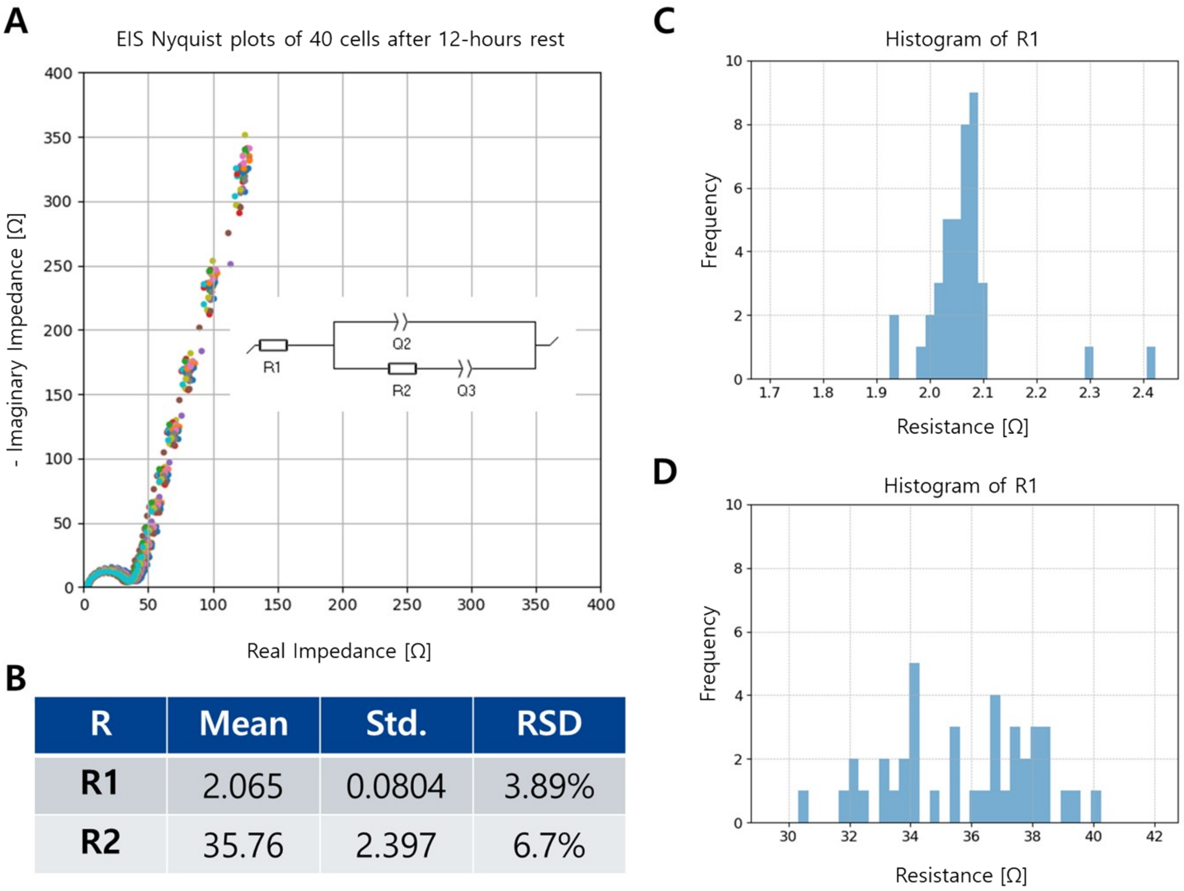

R	Mean	Std.	RSD
R1	2.065	0.0804	3.89%
R2	35.76	2.397	6.7%

Figure S14. EIS results of 40 cells after 12-hours rest. (A) Schematic of the equivalent circuit and Nyquist plots for 40 cells and (B) fitted resistance values. (C, D) Histograms of resistance distribution for different resistance components (R_1, R_2).

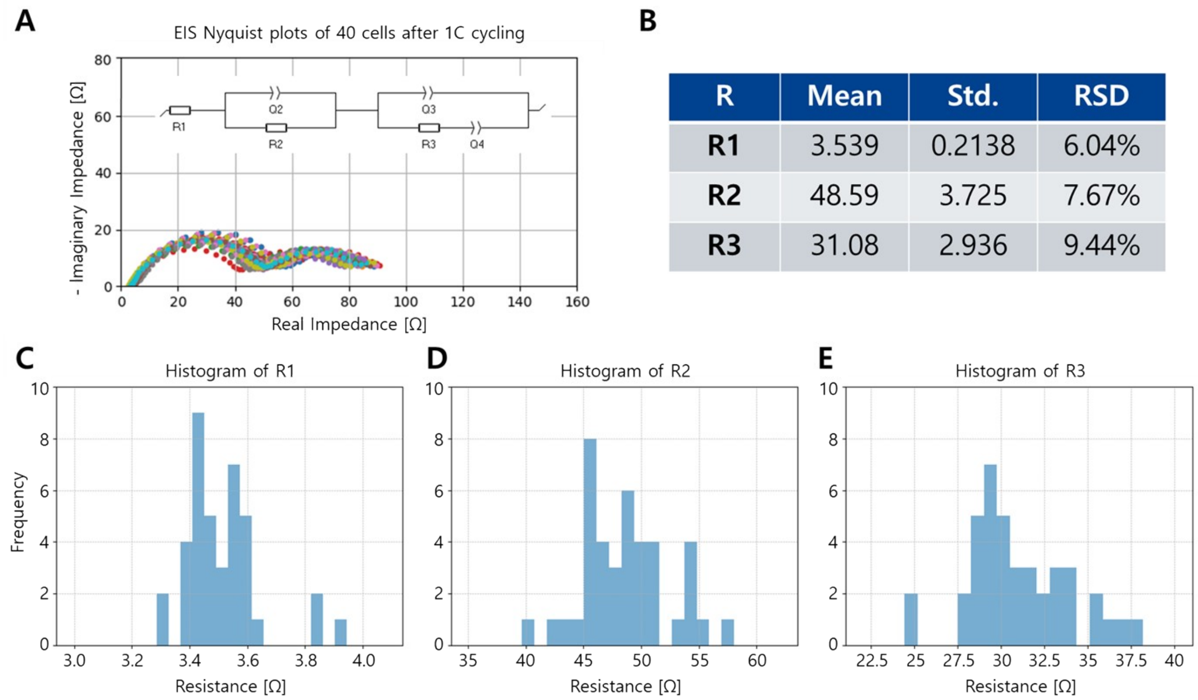

R	Mean	Std.	RSD
R1	3.539	0.2138	6.04%
R2	48.59	3.725	7.67%
R3	31.08	2.936	9.44%

Figure S15. EIS results of 40 cells after 1C-rate cycling. (A) Schematic of the equivalent circuit and Nyquist plots for 40 cells and (B) fitted resistance values. (C-E) Histograms of resistance distribution for different resistance components (R_1, R_2, and R_3).

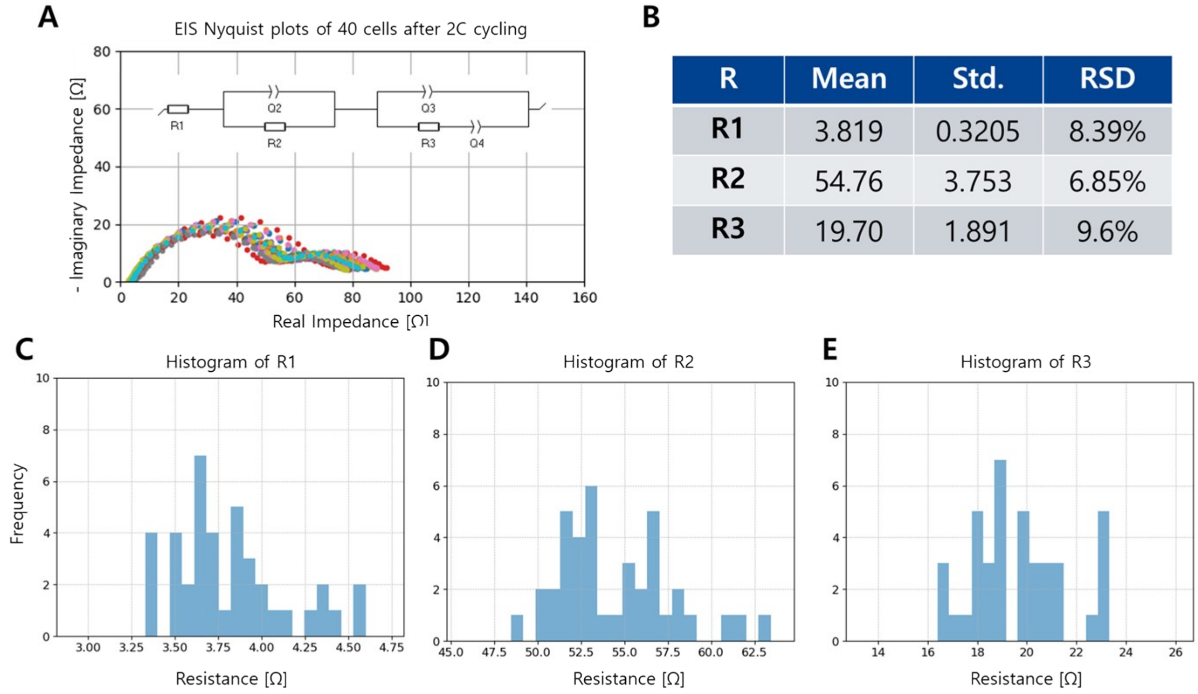

R	Mean	Std.	RSD
R1	3.819	0.3205	8.39%
R2	54.76	3.753	6.85%
R3	19.70	1.891	9.6%

Figure S16. EIS results of 40 cells after 2C-rate cycling. (A) Schematic of the equivalent circuit and Nyquist plots for 40 cells and (B) fitted resistance values. (C-E) Histograms of resistance distribution for different resistance components (R_1, R_2, and R_3).

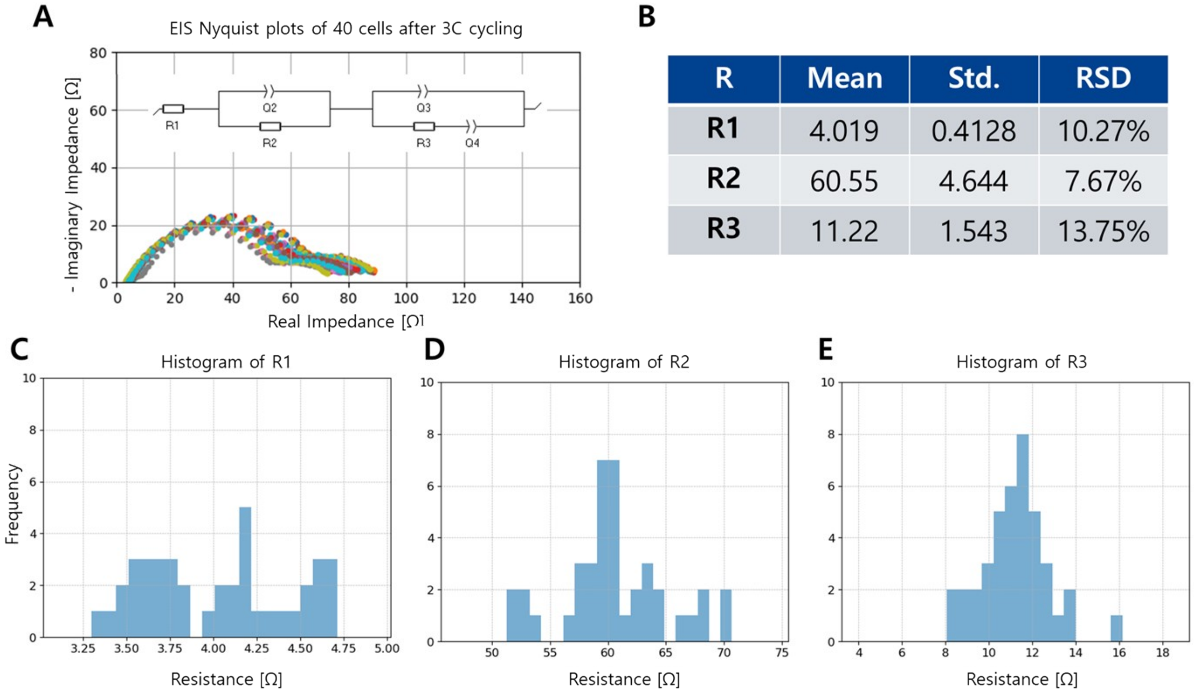

R	Mean	Std.	RSD
R1	4.019	0.4128	10.27%
R2	60.55	4.644	7.67%
R3	11.22	1.543	13.75%

Figure S17. EIS results of 40 cells after 3C-rate cycling. (A) Schematic of the equivalent circuit and Nyquist plots for 40 cells and (B) fitted resistance values. (C-E) Histograms of resistance distribution for different resistance components (R_1, R_2, and R_3).

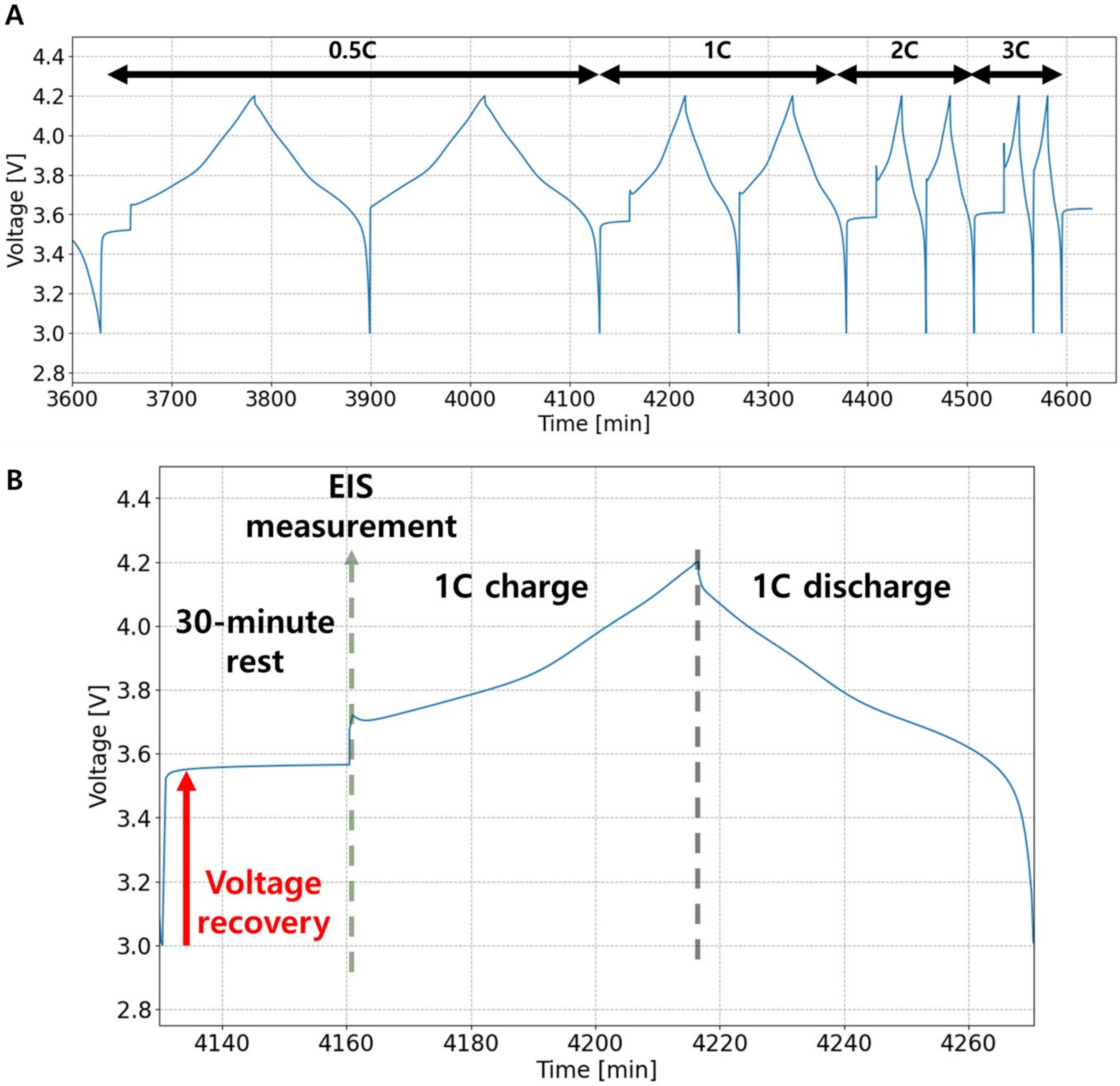

Figure S18. Voltage profile of the cycling protocol used for EIS measurements. (A) Profiles at 0.5C, 1C, 2C, and 3C. (B) Rapid voltage recovery during the rest period following discharge.

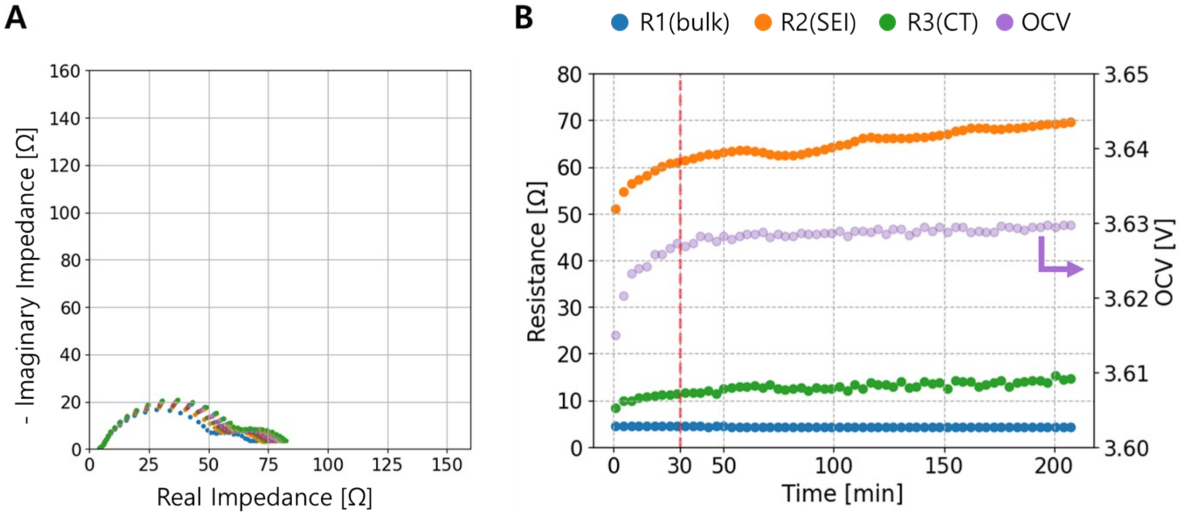

Figure S19. Impedance evolution as a function of rest time after 3C cycling for a single cell. (A) Nyquist plots obtained at different rest times. (B) Resistance and OCV variation over time.

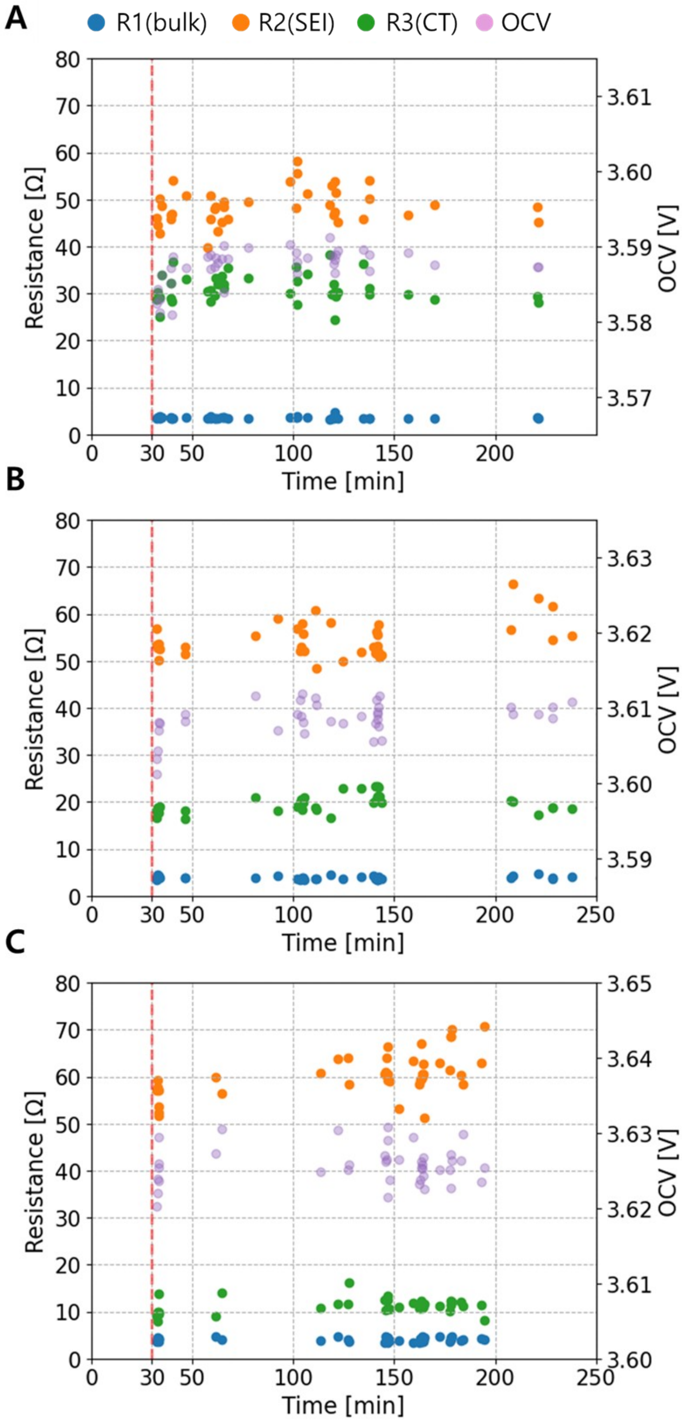

Figure S20. Resistance and OCV variation over time for 40 cells.

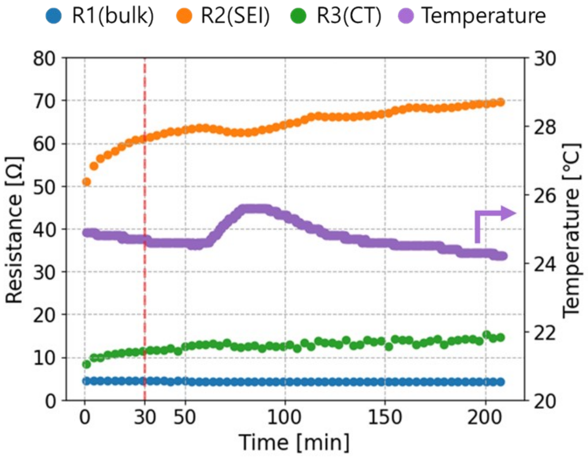

Figure S21. Resistance and ambient temperature variations as a function of rest time after 3C cycling.

Data availability

All the codes, program files and videos for ALBATROSS can be found at https://github.com/Hyun-Gi/ALBATROSS with DOI: https://doi.org/10.5281/zenodo.18959775.